Journal of Materials Chemistry B

PAPER

View Article Online
View Journal | View Issue

Check for updates

Cite this: J. Mater. Chem. B, 2018, 6, 6752

Subcellular co-delivery of two different site-oriented payloads based on multistage targeted polymeric nanoparticles for enhanced cancer therapy†

Chao-Qun You,[ab] Hong-Shuai Wu,[a] Zhi-Guo Gao,[a] Kai Sun,[a] Fang-Hui Chen,[a] W. Andy Tao[c] and Bai-Wang Sun *[a]

Received 23rd August 2018,
Accepted 2nd October 2018

DOI: 10.1039/c8tb02230e

rsc.li/materials-b

The co-delivery of two or more anti-tumor agents using nanocarriers has shown great promise in cancer therapy, but more work is needed to selectively target drugs to specific subcellular organelles. To this end, our research has reported on "smart" polymeric nanoparticles that can encapsulate two different site-oriented pro-drug molecules, allowing them to reach their targeted subcellular organelles based on NIR-mediated controlled release, allowing for targeted modifications in the nucleus or the mitochondria. Specially, an all-*trans* retinoic acid (RA) conjugated cisplatin derivative (RA–Pt) can be delivered with high affinity to the nucleus of target cells, facilitating the binding of cisplatin to double-stranded DNA. Similarly, a synthesized derivative generated by conjugation of triphenylphosphine (TPP) and celastrol (TPP–Cet) may facilitate mitochondrial targeted drug delivery in tumor cells, inducing ROS accumulation and thereby leading to apoptosis. Relative to nanoparticles loaded with a single therapeutic agent, dual antitumor agent-loaded nanocarriers showed promising synergy, exhibiting significant tumor inhibition *in vivo* (81.5%), and less systemic toxicity than the free therapeutic agents alone or the drug-loaded nanoparticles without targeted ligands. These results indicated that site-oriented payloads can effectively enhance antitumor therapeutic efficiency and these studies offer a novel "multistage targeted-delivery" strategy in synergistic therapy for cancer treatment.

1. Introduction

In recent decades, various strategies have been employed for the study of cancer therapy. Nanotechnology in particular has been of great interest in this field, owing to the synthesis, characterization and application of novel nanomaterials with useful properties. The unique advantages of these small materials allow for their potential application to nanoscale biological structure modifications.[1] In recent years, significant advances have been made in the application of nanotechnology to biological and medical fields.[2] A variety of nanostructures including biodegradable polymers, dendrimers, inorganic carbon materials (such as mesoporous silica, and graphene), liposomes, and lipid-based nanocarriers have been developed and have shown great potential in diagnostic and therapeutic applications.[3]

One very advantageous strategy has been to encapsulate therapeutic agents in nanocarriers, enhancing their stability and allowing for targeted delivery and controlled release. These beneficial features allow for improved therapeutic efficacy and significantly decreased toxicity due to a higher localized intratumoral drug concentration.[4–6] Moreover, therapeutic agents such as proteins, peptides, and nucleic acids are better preserved when encapsulated in nanocarriers, as many such molecules are susceptible to enzymatic degradation by nucleases and proteases.[7] However, not all nanocarriers show the expected therapeutic responses when these drug carriers are targeted at the organ-, tissue-, or cellular-level owing to targeting limitations that result in drugs not localizing to the appropriate subcellular compartments (such as the cytosol, mitochondria, or nucleus).[8–10] Therefore, the development of a novel nanomedicine system that can specifically target not only tumor cells of interest, but also specific subcellular compartments is of great interest as such a platform could maximize the therapeutic efficiency of nanocarrier-loaded drug molecules for the treatment of cancer.[11–14]

[a] School of Chemistry and Chemical Engineering, Southeast University, Nanjing 210089, P. R. China. E-mail: chmsunbw@seu.edu.cn; Fax: +86 25 52090614; Tel: +86 25 52090614
[b] College of Chemical Engineering, Nanjing Forestry University, Nanjing 210037, P. R. China
[c] Department of Biochemistry, Purdue University, West Lafayette, Indiana 47907, USA

† Electronic supplementary information (ESI) available: Synthesis procedure of Pt(IV)–COOH, synthetic route for RA–Pt and TPP–Cet, ^{1}H NMR spectra and ESI-MS data of products and other supplementary data. See DOI: 10.1039/c8tb02230e

Of all subcellular organelles, the nucleus is the preferred target for delivery of most therapeutic agents, particularly in the context of cancer because it is the site of DNA replication and is vital for cell proliferation and survival. In general, nuclear localization sequence (NLS)-tagged carriers or drugs are the most common approaches to nuclear targeting.[15,16] However, whereas NLS-tagged peptide ligands are fragile, small chemical molecules are more stable and easier to modify. It has been reported that all-*trans* retinoic acid (RA) can easily bind to cellular retinoic acid-binding protein II (CRABP-II), and this adduct shows excellent affinity for the nuclear RA receptor.[17,18] As it is already widely used in clinical settings, cisplatin is typically the preferred therapeutic agent for many cancers even though it does not show an expected therapeutic response against some tumors. Moreover, cisplatin may cause systemic toxicity, particularly nephrotoxicity, in patients as it can have a high concentration distribution and extended accumulation in kidneys.[19–21] Therefore, the conjugation of RA with cisplatin may allow for the nuclear targeting and delivery of this chemotherapeutic agent in tumor cells, thereby maximizing therapeutic efficacy.

As the key site of cellular energy generation, mitochondria also play a critical role in the homeostasis of various physiological functions including electron transfer and apoptosis.[22,23] A variety of human disorders are caused in part by mitochondrial dysfunction, including diabetes, neuromuscular diseases, and even cancer. A major basis for these symptoms is the overproduction of reactive oxygen species (ROS).[24,25] Thus, a strategy for cancer treatment based on the controlled induction of mitochondrial ROS and disrupted homeostasis exists. Celastrol (Cet), a natural product with a variety of biological activities, has been shown to possess strong antioxidant and antitumor angiogenesis potential. It has been reported that celastrol can induce ROS accumulation by acting on the mitochondrial respiratory chain (MRC) complex I, causing decreased mitochondrial membrane potential and cytochrome *C* release into cytoplasm. Importantly, celastrol can also regulate mitochondrial signaling pathways *via* activating caspase 3 and caspase 9, inducing tumor cell apoptosis.[26–28] Therefore, mitochondrial targeting of celastrol may be a viable therapeutic strategy in tumor cells.

Recently, triphenylphosphonium (TPP), a common chemical molecule, has been shown to have great binding affinity for the inner mitochondrial membrane, and it has therefore been suggested as an optimal candidate for mitochondria targeting of drug conjugates or nanocarriers.[29–35] The high binding affinity of TPP for the inner mitochondrial membrane allows for the delivery of drugs or nanocarriers across the negatively charged mitochondrial membrane due to its highly lipophilic nature and positive charge.[36] Conjugation of TPP with celastrol may therefore facilitate the mitochondrial delivery of this agent in the tumor cells, inducing ROS accumulation in a targeted manner. While this approach shows great promise, further studies are still needed as there are many regulatory barriers to therapeutic molecule delivery.

An important point of note is that the co-delivery of two or more anti-tumor agents simultaneously using nanocarriers has been shown to offer key advantages relative to single agent delivery. Such synergistic treatments can more effectively kill tumor cells by simultaneously blocking apoptotic signaling pathways and inhibiting DNA replication, potentially increasing therapeutic efficacy while reducing the risk of tumor drug resistance.[37–41] To this end, we have designed and synthesized two novel pro-drug molecules (RA–Pt and TPP–Cet) that can specifically target the nuclear and mitochondrial subcellular compartments, respectively. Specially, RA–Pt has a high affinity for the nucleus and can facilitate the binding of cisplatin to double-stranded DNA. The TPP–Cet conjugate may facilitate mitochondrial drug targeting in tumor cells, inducing ROS accumulation and leading to apoptosis. This delivery process can be traced by ICG imaging. To maximize therapeutic efficacy and significantly decrease toxicity, these functional molecules were trapped in folate and cRGD conjugated polymeric nanoparticles, and release was controlled by ICG-mediated photothermal conversion using NIR irradiation. When taken into the cytoplasm by endocytosis, these nanocarriers were depolymerized by the induced heat, and the encapsulated pro-drug molecules were released. The therapeutic efficacy of this prepared functional nano-platform was evaluated using tumor cells *in vitro* and further validated in a breast cancer tumor model of BALB/c nude mice *in vivo*. Our results indicate that site-oriented payloads can effectively enhance chemotherapeutic efficiency, and these studies thus offer a new strategy for multistage targeted delivery and synergistic therapy based on functional nanomedicines.

2. Materials and methods

2.1 Materials

FA–PEG_{2k}–DSPE, $PLGA_{3k}$, and cyclic (Arg-Gly-Asp-D-Phe-Lys) peptide (cRGD) were purchased from Polymtek Biomaterial Co., Ltd (Shenzhen, China). Lecithin, and triphenylphosphine (TPP) were purchased from Sinopharm Chemical Reagent Co., Ltd (China). All-*trans* retinoic acid (RA), indocyanine green (ICG) and celastrol (Cet) were purchased from Sigma-Aldrich Chemical Company (St. Louis, MO, USA). Cisplatin (Pt) was purchased from Shandong Boyuan Pharmaceutical Co., Ltd (Jinan, Shandong, China). cRGD–PEG_{5k}–PCL_{10k} was synthesized according to previously reported procedures.[42] All the dye kits were obtained from Beyotime Biotechnology Co., Ltd (China). All the other chemical reagents were obtained from Sinopharm Chemical Reagent Co., Ltd.

2.2 Instruments

^{1}H NMR spectra were recorded on a Bruker AVANCE III HD-600 spectrometer using deuterated reagents as solvents. TEM images were obtained on a JEM-2100 transmission electron microscope at an acceleration voltage of 100 kV. The UV-vis-NIR absorption and fluorescence emission spectra were measured on a UV-2600 and Shimadzu RF5301PC spectrophotometer, respectively. Hydrodynamic diameters were determined using a Malvern Zetasizer Nano-ZS system at 25 °C. CLSM images were acquired using a LSM700 laser confocal microscope.

Flow cytometry experiments were conducted using a BD LSRFortessa X-20 cell analyzer.

2.3 Synthesis of two site-oriented pro-drug molecules

2.3.1 Synthesis of the all-*trans* retinoic acid conjugate cisplatin compound (RA–Pt). The nuclear targeting molecules (RA–Pt) were obtained from conjugate Pt(IV)–COOH (the synthetic procedure is shown in ESI†) and amino modified all-*trans* retinoic acid (RA–NH_2). At first, the all-*trans* retinoic acid (RA) was modified with amino. Briefly, RA (0.90 g, 3.0 mmol), EDCl (1.15 g, 6.0 mmol), and NHS (0.52 mg, 4.5 mmol) were dissolved in DCM (35 mL) under an ice-water bath and stirring for 2 h, then ethylenediamine (0.36 g, 6.0 mmol) was added and reacted overnight at room temperature. Then the mixture solution was washed with water, extracted with DCM and separated by column chromatography (PE : EA = 3 : 1). The desired intermediate products were obtained after being concentrated and drying under reduced pressure. RA–NH_2 was recovered as a dark yellow solid (0.65 g, 63%). ^{1}H NMR (600 MHz, DMSO-d_6): δ (ppm) 7.93 (d, 1H), 6.91 (d, 1H), 6.31–6.14 (d, 4H), 5.83 (b, 1H), 3.17–3.09 (m, 4H), 2.27 (b, 3H), 2.03–1.94 (b, 5H), 1.69–1.02 (d, 15H). ESI-MS (*m*/*z*): 343.5 $[M + H]^+$.

Next, the conjugation process of RA–Pt was carried out in a similar manner with the EDCl/NHS groups as an activator. Pt(IV)–COOH (1.07 g, 2.0 mmol), EDCl (0.77 g, 4.0 mmol), and NHS (0.35 g, 3.0 mmol) were dissolved in DMF (30 mL) under an ice-water bath and stirring for 2 h, then RA–NH_2 (0.69 g, 2.0 mmol) was added and reacted overnight at room temperature. The desired products were obtained after solvent evaporation under reduced pressure and then washed with deionized water, and ethanol in turn. The crude product was purified from methanol and dried under vacuum to give the desired product as a yellow solid (0.79 g, 46%). ^{1}H NMR (600 MHz, DMSO-d_6): δ (ppm) 7.99 (d, 1H), 6.93–6.88 (d, 1H), 6.31–6.15 (d, 4H), 5.81 (b, 1H), 3.29–3.16 (m, 5H), 2.91–2.54 (b, 2H), 2.47–2.20 (b, 6H), 2.05–1.91 (b, 7H), 1.72–1.01 (d, 17H). ESI-MS (*m*/*z*): 858.3 $[M + H]^+$.

2.3.2 Synthesis of the triphenylphosphine conjugate celastrol compound (TPP–Cet). The mitochondrial targeting molecules (TPP–Cet) were obtained from the conjugation of TPP–NH_2 and celastrol with a similar amination reaction. Besides, the triphenylphosphine (TPP) was modified with amino. Briefly, TPP (1.29 g, 3.0 mmol), EDCl (1.15 g, 6.0 mmol), and NHS (0.52 g, 4.5 mmol) were dissolved in DCM (40 mL) under an ice-water bath and stirring for 2 h, then ethylenediamine (0.36 g, 6.0 mmol) was added and reacted overnight at room temperature. Next, the mixture solution was washed with water, extracted with DCM and separated by column chromatography (PE : EA = 1 : 1). The desired intermediate products were obtained after being concentrated and drying under reduced pressure. TPP–NH_2 was recovered as a white powder (0.74 g, 54%). ^{1}H NMR (600 MHz, DMSO-d_6): δ (ppm) 7.94–7.67 (dt, 6H), 7.58–7.39 (dt, 4H), 7.31–7.05 (dt, 6H), 3.58–3.46 (b, 1H), 3.34–3.27 (b, 1H), 2.76–2.66 (b, 1H), 2.11–1.87 (b, 1H), 1.84–1.60 (b.1H), 1.31–1.19 (b, 2H). ESI-MS (*m*/*z*): 471.1 $[M + H]^+$.

Next, the conjugation process of TPP–Cet was carried out in a similar way. Briefly, celastrol (0.90 g, 2.0 mmol), EDCl (0.77 g, 4.0 mmol), and NHS (0.35 g, 3.0 mmol) were dissolved in DCM (30 mL) under an ice-water bath and stirring for 2 h, then TPP–NH_2 (1.41 g, 3.0 mmol) was added and reacted overnight at room temperature. Then the mixture solution was washed with water, extracted with EA and separated by column chromatography (PE : EA = 3 : 2). The obtained crude products were purified from ethanol and dried under vacuum to give the desired product as a palm red solid (0.78 g, 43%). ^{1}H NMR (600 MHz, DMSO-d_6): δ (ppm) 7.84–7.70 (dt, 7H), 7.51–7.44 (dt, 5H), 7.26–7.13 (dt, 8H), 6.59 (b, 1H), 6.42–6.33 (d, 1H), 5.91–5.84 (b, 1H), 2.86–2.77 (d, 4H), 2.55–1.93 (d, 13H), 1.71–0.54 (d, 36H). ESI-MS (*m*/*z*): 903.4 $[M + H]^+$.

2.4 Formation of folate and cRGD modified RA–Pt and TPP–Cet loaded nanoparticles (RA–Pt/TPP–Cet@Fc-INPs)

The designed drug carriers were prepared using a thin film hydration method. Briefly, FA–PEG_{2k}–DSPE (1.0 mg), cRGD–PEG_{5k}–PCL_{10k} (1.0 mg), $PLGA_{3k}$ (10.0 mg) and lecithin (30.0 mg) were dissolved in chloroform (40 mL) and a thin film was formed after solvent evaporation under reduced pressure. To this film was added 15 mL of RA–Pt aqueous solution (0.2 mg mL^{-1}), 10 mL of TPP–Cet aqueous solution (0.3 mg mL^{-1}), and 5 mL of ICG aqueous solution (0.4 mg mL^{-1}) and it was ultrasonically vibrated for 8 min. The prepared nanoparticle suspension was then centrifuged at 3000 rpm for 15 min and the supernatant was then filtrated through a 0.22 μm cellulose acetate filter membrane and lyophilized. The obtained solid powder was re-dissolved in CH_3OH and characterized with UV-vis spectroscopy.

2.5 Photothermal effects and *in vitro* drug release

To evaluate the photothermal conversion induced by ICG, several different concentrations of RA–Pt/TPP–Cet@Fc-INP nanoparticle suspension (0.2, 0.4, and 0.8 mg mL^{-1}) were analyzed after irradiation with an 808 nm near-infrared laser (1.54 W) for 5 min. Next, we investigated the thermal efficiency of the ICG loaded nanoparticles. The temperature variation of the nanoparticle suspension was detected with an infrared (IR) thermal camera. Before the evaluation, five cycles of irradiating and chilling processes were tested to evaluate the photostability.

The drug release investigation of RA–Pt/TPP–Cet@Fc-INPs was performed using a dialysis method as our previous work described.[43,44] A predetermined amount of the prepared nanoparticles (3 mL, 1.5 mg mL^{-1}) in dialysis tubing (MW, 15 000) was immersed in phosphate buffered saline (PBS, PH = 7.4, 6.8 and 5.5) as dissolution media. The release investigation was performed with near-infrared laser (808 nm, 1.54 W, 5 min) irradiation (+, −). At designed time intervals, a certain volume (2 mL) of the release medium was taken out and the fluorescence emission intensity at 425 nm under an excitation wavelength of 280 nm was determined by the fluorescence spectrometer to calculate the amount of TPP–Cet, while an equal volume (2 mL) of fresh PBS was added to proceed with the release. The amount of RA–Pt presented in the dialysate was calculated by ICP-AES. The release experiments were tested in triplicate, and the mean value was calculated as the final result.

2.6 Cellular uptake study

In breast cancer, as an infinite tumor with extremely high incidence, the expression level of $\alpha_v\beta_3/\alpha_v\beta_5$ in MDA-MB-231 cells is very high, while the expression level of folate receptor in MCF-7 cells is relatively higher.[45–48] Thus, we choose these two kinds of cells to study the targeted delivery of folate and cRGD modified drug-loaded nanoparticles we prepared.

Human breast cancer cells (MDA-MB-231 and MCF-7) were cultured with Dulbecco's modified Eagle medium (DMEM) containing 10% fetal bovine serum (FBS) and 1% penicillin–streptomycin solution under 5% CO_2 atmosphere at 37 °C. In the CLSM study, MDA-MB-231 and MCF-7 cells were severally seeded in a confocal culture dish (2 mL medium) at a density of 8.0×10^4 cells per dish. After being cultured under 5% CO_2 atmosphere at 37 °C for 24 h, a predesigned amount of RA–Pt/TPP–Cet@Fc-INP nanoparticle suspension (2 mL) with an equivalent ICG concentration of 50.0 μg mL^{-1} was added into the cell culture medium. After further incubation for 1, 3, and 12 h, the culture medium was removed, and the cells were washed three times with PBS. Then, the cells were stained with Hoechst 33258 and further mounted for observations with CLSM. In addition, MCF-7 cells treated with the prepared nanoparticle conjugate targeted ligands (Fc-INPs) or not (INPs) were also incubated to evaluate the receptor-mediated endocytosis. Finally, the fluorescence intensity of the cellular uptake was calculated using a flow cytometer and the intracellular RA–Pt was quantitated by ICP-AES.

2.7 Nuclear targeting and quantification of RA–Pt

The experimental process of nuclear targeting evaluation was performed as described above. MCF-7 cells were seeded in a confocal culture dish (2 mL medium) at a density of 8.0×10^4 cells per dish. After being cultured for 24 h (at 37 °C, 5% CO_2), RA–Pt and ICG loaded nanoparticle conjugate RA ligand (RA–Pt@RA-INPs) or not (RA–Pt@INPs) suspensions (2 mL) with an equivalent RA–Pt concentration of 47.0 μg mL^{-1} were added into the confocal culture dish. After further incubation for 6 h, the waste was removed, and the cells were washed three times with PBS. Then the cells were stained with DAPI (nucleus staining, blue color) and further observed with CLSM. Besides, quantification was performed with the same procedures of cell incubation and we also added the RA–Pt/TPP–Cet@Fc-INP group with the same RA–Pt dosage (47.0 μg mL^{-1}, 2 mL). After been incubated for 6 h, the cells were then trypsinized and suspended at a concentration of 5×10^6 cells per mL for 10 min at 4 °C in 1% Triton X-100 solution (0.1 M NaCl, 1 mM EDTA, 10 mM Tris buffer, pH 7.4). The suspension was further centrifuged (15 min, 1000 rpm), and the pellets (nuclei) were separated from the supernatant (cytosol).[49] Finally, the collected precipitation was washed and determined by ICP-AES.

2.8 Mitochondria targeting and ROS generation in cells

All the experimental procedures in this section for observation were consistent with those in the nuclear targeting investigation. Specifically, the cells were incubated with ICG loaded nanoparticles (ICG: 38.2 μg mL^{-1}, 2 mL) conjugate TPP (INPs) or not (TPP-INPs). Finally, the cells were stained with Lysotracker Green (lysosome staining, green color) and observed with CLSM. Next, the induced singlet oxygen was generated by TPP–Cet to further achieve synergistic therapy and the intracellular ROS were detected by an oxidation-sensitive fluorescent probe (DCFH-DA).[50] Similarly, MCF-7 cells was seeded in 6-well plates and further incubated for 12 h after being treated with celastrol and ICG loaded, folate and cRGD modified nanoparticles (Cet@Fc-INPs); TPP–Cet and ICG loaded, folate and cRGD modified nanoparticles (TPP–Cet@Fc-INPs); and RA–Pt, TPP–Cet and ICG loaded, folate and cRGD modified nanoparticles (RA–Pt/TPP–Cet@Fc-INPs) (celastrol: 48.3 μg mL^{-1}; ICG: 38.2 μg mL^{-1}, 2 mL). Then DCFH-DA (10.0 μM) was employed to measure the ROS by celastrol. Finally, the fluorescence intensity of ROS production in MCF-7 cells was acquired by a flow cytometer with excitation at 488 nm.

2.9 *In vitro* cytotoxicity study

To evaluate the synergistic therapy of two different pro-drug molecules, MDA-MB-231 and MCF-7 cells were seeded in 96-well plates (100 μL medium) and incubated overnight. When the cell confluence reached around 70%, the medium was replaced with fresh DMEM containing different formulations of nanoparticle suspensions with various RA–Pt concentrations (0.1, 0.5, 1.0, 5.0, 10.0 μg mL^{-1}, equivalent to Pt: 0.03, 0.17, 0.30, 1.70, 3.00 μg mL^{-1}) added; the concentration of TPP–Cet is calculated as the ratio of nanoparticles to RA–Pt. After 12 h of incubation, the medium was replaced, and the cells were further irradiated with an 808 nm NIR laser (1.54 W, 3 s $well^{-1}$).[51] After being incubated for 3 h, the cells were further irradiated by 670 nm near-infrared light for 10 minutes and then incubated for 9 hours. After the incubation for 24 h in total, the standard MTT assay was performed to evaluate the cell viability.

2.10 Animal experiments and tumor models

Female BABL/c nude mice (each 18–22 g) were purchased from Shanghai Lingchang Biotechnology Co. LTD (Shanghai, China) and raised under the principles of care and use of laboratory animals. The MCF-7 tumor models were generated by subcutaneous injection of 100 μL cell suspension (in saline medium, 1×10^7 cells mL^{-1}) into the right flank of each mouse. After incubation for 12 days, the mice were used for further experiments when the tumor size had grown to ~60 mm^3. All animal experiments were performed under the guidance approved by the Laboratory Animal Ethics Committee at the School of Medicine, Southeast University (Nanjing, China).

2.11 *In vivo* imaging and biodistribution analysis

The nude mice were randomly divided into two groups (three per group). Mice in group 1 as a control were injected with 200 μL of ICG loaded nanoparticles without targeted ligands (INPs) *via* their tail veins. Mice in group 2 were injected with 200 μL of ICG loaded folate and cRGD conjugate NPs (Fc-INPs, both containing 50 μg mL^{-1} ICG) *via* their tail veins. Images and FL quantitative analysis of ICG were taken at 0, 1, 3, 6, 12,

and 24 h after injection using the *ex/in vivo* imaging system (CRI maestro, USA) with a 704 nm excitation wavelength and a 735 nm filter to collect the FL signals of ICG. The mice were sacrificed 24 h after injection and organs including the heart, liver, spleen, lung, kidneys and tumor were collected for imaging and quantitative biodistribution analysis.

2.12 *In vivo* antitumor efficacy studies in the breast cancer model

MCF-7 tumor-bearing mice were divided into 5 groups to determine the tumor growth rate. For the treatment groups (n = 6 per group), mice bearing MCF-7 tumors were injected with 200 μL of PBS (group 1), free RA–Pt (group 2), RA–Pt/TPP–Cet and ICG loaded nanoparticles (RA–Pt/TPP–Cet@INPs, group 3), and RA–Pt/TPP–Cet and ICG loaded, folate and cRGD modified nanoparticles (RA–Pt/TPP–Cet@Fc-INPs, group 4) (containing 150 μg mL^{-1} of RA–Pt solution, equivalent to Pt: 0.52 mg kg^{-1} per mouse; Cet: 0.75 mg kg^{-1} per mouse) *via* their tail veins and group 5 was RA–Pt/TPP–Cet@Fc-INPs irradiated by an 808 nm NIR laser (1.54 W, 5 min) after incubation for 48 h. Each group was injected a total of five times (once every 3 days). For the control group, mice were treated with the same volume of PBS without NIR irradiation. The tumor sizes were measured by an electronic digital caliper every three days after treatment and calculated as follows: tumor volume (TV) = 0.5 × (tumor length) × (tumor width)^2. The relative tumor volumes (RTV) were normalized to their initial sizes. To further detect the effect of enhanced antitumor therapy *in vivo*, the tumors, livers and kidneys at 24 d after treatment were stained with hematoxylin and eosin.

2.12.1 Statistical analysis. Data are expressed as mean ± SD. The differences among groups were determined using one-way ANOVA analysis followed by Tukey's post-test; a P value of <0.05 was considered significant. Statistical significance was defined as $^*P < 0.05$, $^{**}P < 0.01$, and n.s. $P > 0.05$.

3. Results and discussion

3.1 Synthesis and characterization

To obtain the subcellular targeting effect, two novel pro-drug molecules RA–Pt and TPP–Cet were designed and synthesized in the present work. The synthesis route is shown in Fig. S1 (ESI†). The major amination reaction was controlled with the EDCl/NHS group as an activator, which showed high product yield. The chemical structures of the two pro-drug molecules and the intermediates were confirmed by standard spectroscopic techniques including ^{1}H NMR and ESI-MS, and the results are exhibited in Fig. S2–S5 (ESI†). The chemical displacement of each proton exactly appeared on the ^{1}H NMR data images and the molecular ion peaks in ESI-MS results were consistent with the designed compounds, which have fully confirmed the successful synthesis of RA–Pt and TPP–Cet.

3.2 Self-assembly behavior

Next, the RA–Pt and TPP–Cet dual-loaded functional nanoparticles (RA–Pt/TPP–Cet@Fc-INPs) were prepared and the assembly instruction are shown in Scheme 1. The FA–PEG$_{2k}$–DSPE, and cRGD–PEG$_{5k}$–PCL$_{10k}$ chains were synthesized and self-assembled as our previous work described.[52] We have tested various proportional combinations of FA–PEG$_{2k}$–DSPE, cRGD–PEG$_{5k}$–PCL$_{10k}$, lecithin, and PLGA$_{3000}$ to obtain excellent overall performance of drug carriers (Table S1, ESI†). The DLS results (Fig. 1B) showed a pleasing particle size of 99.65 nm with a harmonious polydispersity of 0.261, while it was about 131.20 nm (Fig. 1A) before conjugating with targeted ligands. We further verified that the particle size was only 79.88 nm (Fig. S6, ESI†) before encapsulating drug molecules. According to reports,[53,54] if the particle size of the nanoparticles is too small or too large they can easily be filtered by the kidney or swallowed by Kupffer cells in the liver. In addition, nanoparticles with a particle size of

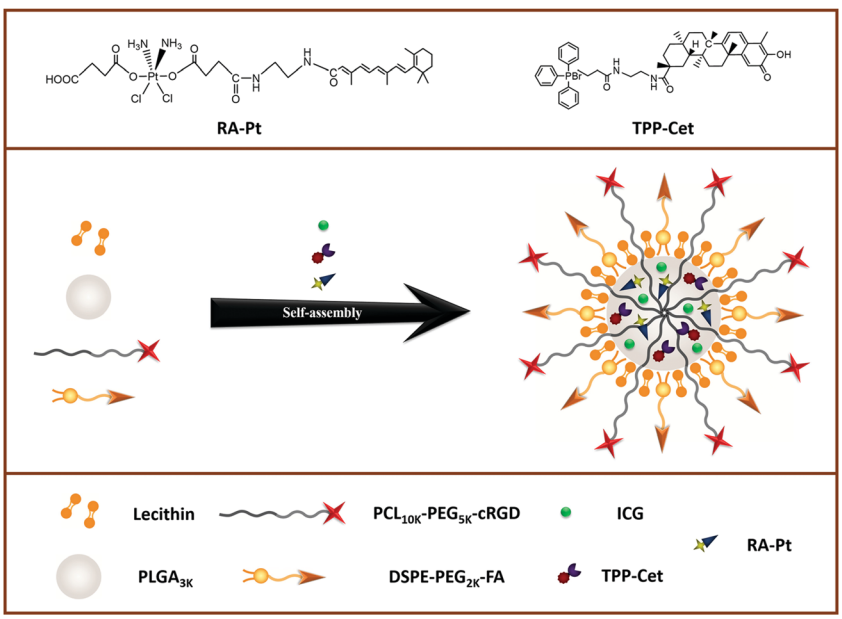

Scheme 1 Self-assembly of folate and cRGD dual-targeted polymeric nanoparticles loaded with RA–Pt and TPP–Cet.

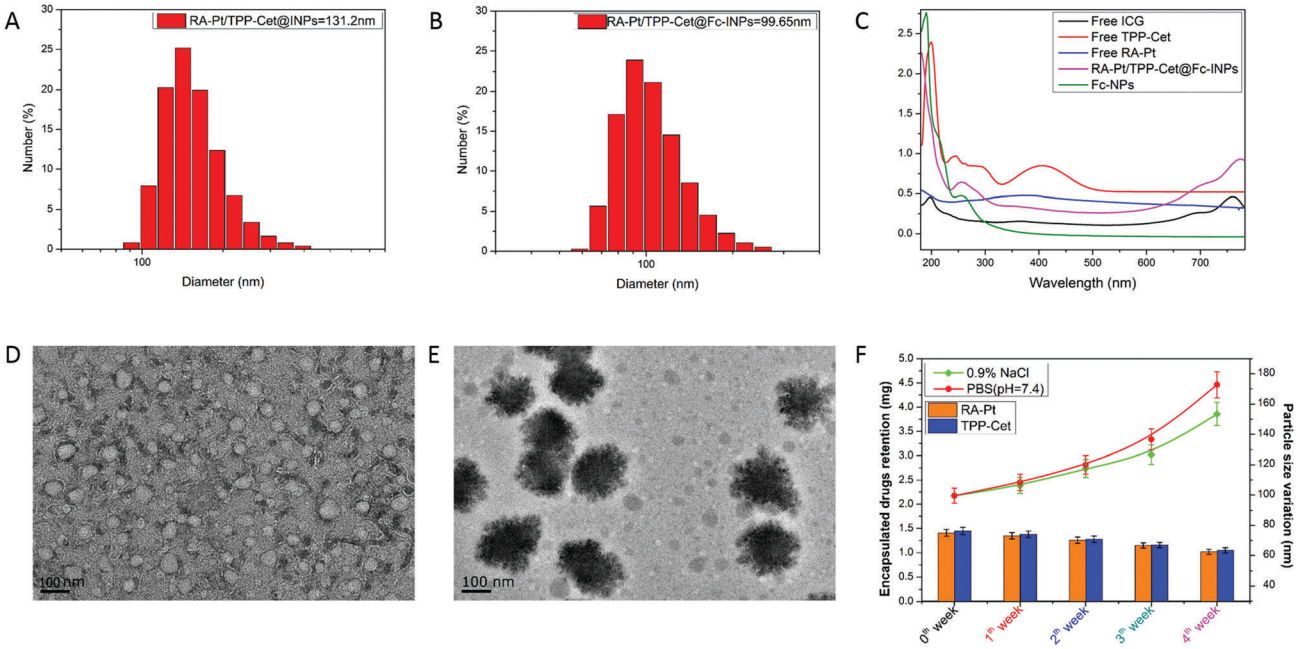

Fig. 1 (A) Size distribution of RA–Pt and TPP–Cet loaded nanoparticles without folate and cRGD ligands (RA–Pt/TPP–Cet@INPs). (B) Size distribution of RA–Pt and TPP–Cet loaded targeted nanoparticles (RA–Pt/TPP–Cet@Fc-INPs). (C) UV-vis-NIR spectra of ICG in methanol, free TPP–Cet, free RA–Pt, Fc-NPs and RA–Pt/TPP–Cet@Fc-INP suspensions in phosphate buffer (pH = 7.4). (D) TEM images of RA–Pt/TPP–Cet@Fc-INPs in PBS (pH = 7.4) at 25 °C. (E) TEM images of RA–Pt/TPP–Cet@Fc-INPs in PBS (pH = 7.4) with NIR irradiation for 3 min. (F) The drug retention profile and particle size variation under normal conditions during four weeks (PBS or 0.9% NaCl).

about 100 nm have better drug loading capacity and they will not be cleared by the body during blood circulation.[55,56] Thus, the present nanoparticles with a particle size of 99.65 nm showed great potential in nanomedicines. The results further exhibited the ζ potential on the surface of NPs decreased from −24.93 to −49.97 mV after conjugating NPs with folate and cRGD.

The nanoparticles without targeted ligands showed poor dispersion with a polydispersity index of 0.440, which is potentially due to the imbalance of the potential on the surface of the nanoparticles. The introduction of the targeted ligands well regulates the balance of the nanoparticles' surface potential in the aqueous solution, resulting in a good dispersion pattern. The TEM images further exhibited the morphological characteristics of the present folate and cRGD modified nanoparticles under normal conditions (Fig. 1D). The individual dispersion form was still clearly visible though the relatively rough surface may be due to conjugation with targeted ligands. The depolymerized state of the nanoparticles when exposed to the NIR laser indicated the prepared nanoparticles showed highly controllable release (Fig. 1E).

To study the influence of morphological characteristics on the colloidal stability of the prepared nanoparticles, we investigated the drug release profile and particle size variation under normal conditions during four weeks (Fig. 1F). The results indicated the release rate of encapsulated drugs during four weeks was acceptable (RA–Pt, 27.66%; TPP–Cet, 27.59%) while the particle size increased from 99.65 nm to 153.40 and 172.80 nm (in 0.9% NaCl and pH = 7.4 PBS, respectively). Thus, the obtained nanoparticles showed acceptable stability in blood circulation, avoiding the revealing of encapsulated drugs over a period of time.

We further use UV-vis spectroscopy to determine the RA–Pt and TPP–Cet loading amounts of the prepared nanoparticles. The absorption spectra of free ICG, free TPP–Cet, free RA–Pt, folate and cRGD modified hollow nanoparticles (Fc-NPs), and RA–Pt/TPP–Cet@Fc-INPs are shown in Fig. 1C. The spectrum did not show obvious characteristic absorbance for RA–Pt, while the free ICG, free TPP–Cet and Fc-NPs had maximum characteristic absorption peaks around 760, 409, and 259 nm in the UV spectrum, respectively. The chemical shift of protons at each position of coupled amphiphilic copolymer chains was characterized by ^{1}H NMR as shown in Fig. S7 and S8 (ESI†). The characteristic peaks of the benzene ring CH on cRGD at δ 7.15–8.11 ppm obviously appeared in the picture of cRGD–PEG_{5k}–PCL_{10k} at 7.16–7.89 ppm while the PEG_{5k}–PCL_{10k} showed nothing in this region, which confirmed the conjugation of cRGD. The characteristic peaks of the folate at δ 4.55–11.48 ppm obviously appeared in the picture while the HOOC–PEG_{2k}–DSPE showed nothing in this region, which confirmed the conjugation of folate. Therefore, the obtained results indicated that FA and cRGD had been successfully conjugated with NPs.

3.3 Photothermal effects and drug release

To evaluate the impact of ICG mediated photothermal conversion on drug release, the photothermal conversion performance of RA–Pt/TPP–Cet@Fc-INPs was investigated and the results are

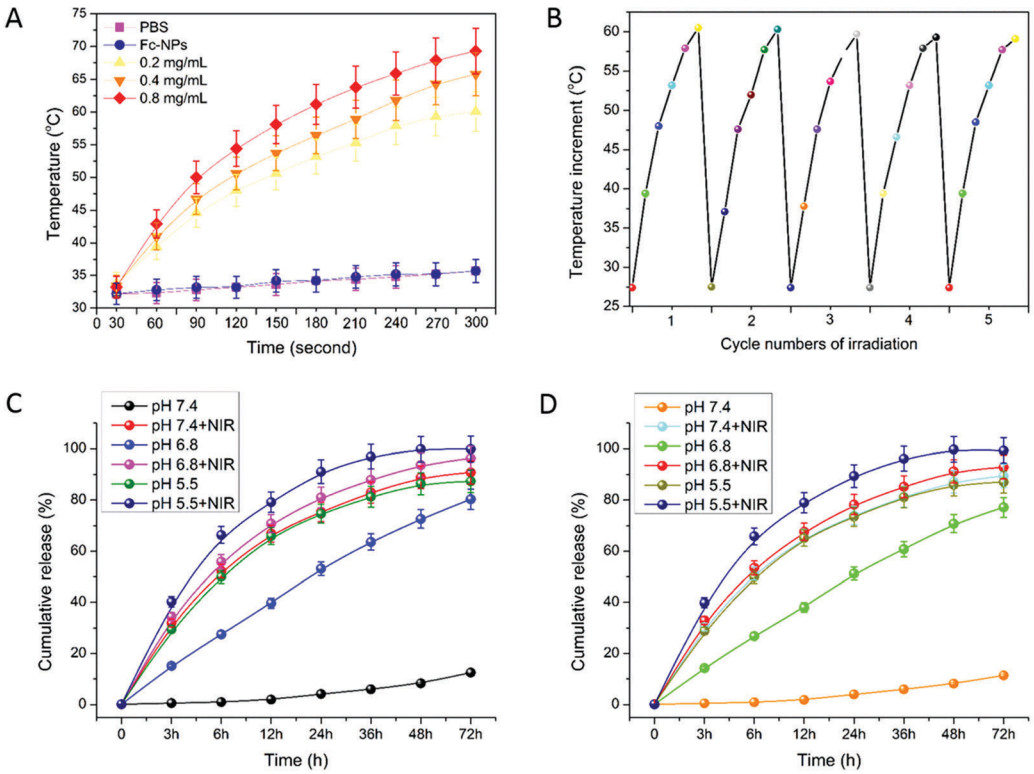

Fig. 2 (A) Heating curves of phosphate buffer (pH = 7.4), hollow nanoparticles (Fc-NPs, 0.8 mg mL^{-1}), and different concentrations of RA–Pt/TPP–Cet@Fc-INPs (0.2, 0.4, and 0.8 mg mL^{-1}) suspended in phosphate buffer (pH = 7.4) under 808 nm laser irradiation at a power of 1.54 W. (B) Temperature increments of the RA–Pt/TPP–Cet@Fc-INP suspension (0.5 mg mL^{-1}) under 808 nm laser irradiation at a power of 1.54 W for five cycles (5 min of irradiation for each cycle). NIR-dependent release of drugs (C, RA–Pt; D, TPP–Cet) from the RA–Pt/TPP–Cet@Fc-INPs at different pH (7.4, 6.8, and 5.5).

shown in Fig. 2. As the results exhibited (Fig. 2A), neither the PBS nor the hollow nanoparticles (Fc-NPs) showed obvious temperature change and the inner temperature was still lower than 35 °C. Next, the induced temperature of RA–Pt/TPP–Cet@Fc-INP suspensions at various concentrations (0.2, 0.4, and 0.8 mg mL^{-1}) was recorded and the results showed a typical concentration-dependent temperature increase. In addition, the fastest temperature increase was observed at the concentration of 0.8 mg mL^{-1}, and the temperature increased by 69.3 °C after exposure to the NIR laser for 5 min. The induced hyperthermia can effectively accelerate drug release or even lead to tumor ablation. In addition, the light stability of RA–Pt/TPP–Cet@Fc-INPs was also tested and the results showed the induced temperature decreased by only 1.4 °C, thus it exhibited excellent photostability of the present nanoparticles (Fig. 2B). Based on the excellent photostability of RA–Pt/TPP–Cet@Fc-INPs, they also could be used as a suitable photothermal agent for sustained photothermal therapy of tumors.

Considering the acid condition inside the tumor cells accelerates the degradation of the shell structure of drug carriers, RA–Pt/TPP–Cet@Fc-INPs were suspended in deionized water (2.0 mg mL^{-1}) and then immersed in PBS with different pH values. Furthermore, 4.70% of RA–Pt and 4.83% of TPP–Cet in the prepared nanoparticles was released in 72 h (over 99.00%) in the presence of a 1.54 W NIR laser (Fig. 2C and D). In contrast, only about 12.55% (or 11.41%) of loaded RA–Pt (or TPP–Cet) was liberated from the NPs at pH = 7.4 without irradiation. The drug release profile implied that the drugs can efficiently be released from the RA–Pt/TPP–Cet@Fc-INPs *via* NIR irradiation. In addition, the water solubility of RA–Pt is better than that of TPP–Cet, in this way, the release rate of RA–Pt is slightly faster than TPP–Cet.

The polymer and lecithin mixture enhanced the stability of the lipid bilayer structure of the prepared nanoparticles, which shows a compact arrangement in the normal environment. However, it depolymerized to a looser structure rapidly due to the intracellular acidic conditions. In addition, the lipid bilayer structure of the nanoparticles suffered more heavily destruction and further collapsed while increasing the temperature by NIR irradiation.

3.4 Intracellular uptake

The crucial factor for tumor treatment is to efficiently delivery drug molecules into the cytoplasm or nucleus. It is well known that folate receptor (FR), a glycosylphosphatidylinositol (GPI)-anchored membrane glycoprotein, is frequently overexpressed on the surface of a variety of tumor cells. In addition, the cyclic Arg-Gly-Asp (cRGD) peptide ligand is able to specifically adhere to $\alpha_v\beta_3/\alpha_v\beta_5$ integrins, which are also overexpressed on various tumor cells and the surface of tumoral endothelial cells.[57] The enhanced cellular uptake of folate and cRGD modified nanoparticles was confirmed by confocal laser scanning microscopy

(CLSM). As expected, FA and cRGD modified nanoparticles were significantly internalized by both tumor cells (Fig. 3A), and the cellular internalization of the nanoparticles showed an obvious time-dependent increase. MCF-7 cells treated with the prepared nanoparticles exhibited stronger fluorescence intensity than that in the MDA-MB-231 cells after being incubated for 12 h. The fluorescence signals mainly gathered surrounding the cell nuclei, indicating the prepared nanoparticles were entrapped inside the lysosome vesicles.[58]

The flow cytometric fluorescent quantitation further confirmed that FA and cRGD dual modification significantly accelerated the internalization of the nanoparticles due to the conjugated targeted ligands. Fig. 3B showed the fluorescent quantitation of MDA-MB-231 and MCF-7 cells at three time intervals (1 h, 3 h, and 12 h). As exhibited, about 1.11-fold higher fluorescence intensity was found in MCF-7 cells than that detected in MDA-MB-231 cells when incubating for 3 h, while the fluorescence intensity in both cells showed no significant difference (FL intensity rate = 1 : 1.13) after incubation for 12 h. We further quantitated the total amount of RA–Pt entering the cells and the results are consistent with the data of FL intensity cumulated in the cells (Fig. 3C).

For quantitative analysis of the cellular uptake amount of receptor-mediated endocytosis, MCF-7 cells were incubated in the medium with ICG loaded nanoparticles conjugated with folate and cRGD ligands (Fc-INPs) or not (INPs) for 6 h and the results are shown in Fig. S9 (ESI†). As expected, about 1.53-fold higher fluorescence intensity was found in Fc-INP treated MCF-7 cells than that in the cells treated with INPs. To a certain extent, the cellular uptake amount of the nanoparticles was accelerated due to the specific interaction between folate, cRGD and their receptors. According to reports, FA modification can strongly accelerate the nanoparticles although it insignificantly increased the total amount of nanoparticles entering the cells.[59] Thus, our obtained results were consistent with the conclusion.

3.5 RA potentiates the nuclear transport of RA–Pt

For the study of nuclear-targeted delivery, we calculated the total amount of RA–Pt entering the nuclear and the results are shown in Fig. 4. Compared to the RA–Pt@INP group (without RA targeting), the red fluorescence signals detected in the nucleus were much stronger in the RA–Pt@RA-INP group (Fig. 4A). On account of the uses of ICGs (one was for tracing drugs), the accumulated amount of RA–Pt was consistent with the fluorescence intensity. Thus, RA also promoted the localization of nanoparticles in the nucleus. Subsequently, we quantified the RA–Pt content in the nucleus (Fig. 4B). Compared with the total amount of RA–Pt (13.48 μg) in MCF-7

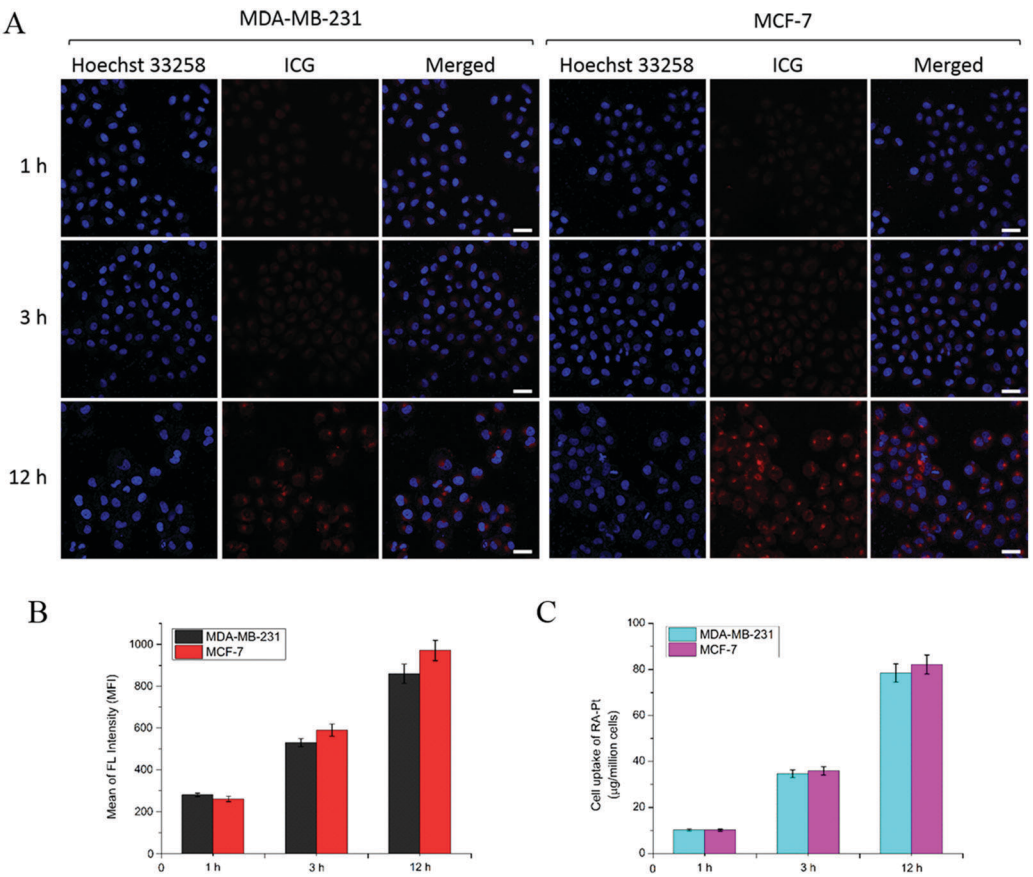

Fig. 3 Intracellular uptake of RA–Pt@Fc-INPs. (A) CLSM images of MDA-MB-231 and MCF-7 cells incubated with the nanoparticles for different periods of time at an equivalent ICG concentration of 50 μg mL^{-1} (scale bar, 40 μm). (B) Flow cytometric analysis of the ICG fluorescence intensity in MDA-MB-231 and MCF-7 cells. (C) Quantitative uptake analysis of RA–Pt in MDA-MB-231 and MCF-7 cells using the ICP-AES instrument.

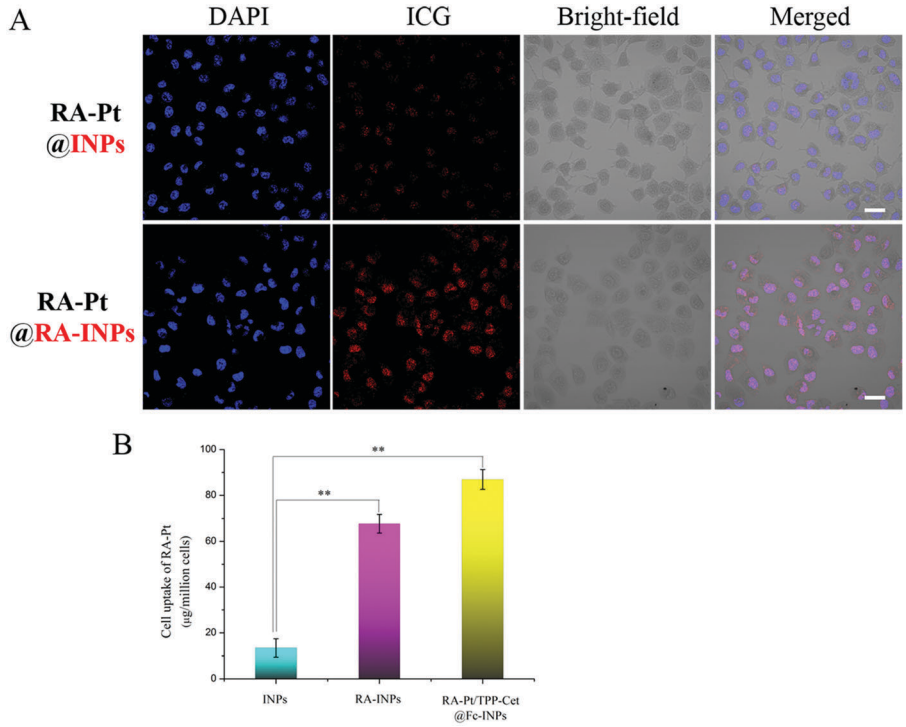

Fig. 4 (A) Internalization of the ICG-labeled targeted nanoparticles (RA–Pt@RA-INPs) or nanoparticles without RA ligands (RA–Pt@INPs) (equivalent to 47.0 μg mL^{-1} RA–Pt) by MCF-7 cells for 6 h, analyzed by CLSM (scale bar, 40 μm). (B) Quantitative measurement of the RA–Pt content in the nucleus after incubating MCF-7 cells for 6 h with RA–Pt loaded nanoparticles (equivalent to 47.0 μg mL^{-1} RA–Pt) in the presence or absence of RA. Data are presented as the mean ± SD (n = 3, *P < 0.05, **P < 0.01).

cells when treating with RA–Pt@INPs, the cellular uptake amount in the RA–Pt@RA-INP group increased to 67.73 μg in 6 h, which exhibited an infusive cellular uptake efficiency. The amount of accumulated RA–Pt in the nucleus in the RA-INP group was 5.02-fold that in the INP group (P < 0.01). Likewise, the amount of accumulated RA–Pt in MCF-7 cells when treating with RA–Pt/TPP–Cet@Fc-INPs increased to 86.97 μg, which reaches 92.52% of the total input. Thus, RA enabled cisplatin to deliver from cytosol to the nucleus more efficiently and enhanced the accumulation in the nucleus.

3.6 Mitochondria targeting and ROS generation in cells

Similarly, we further evaluated the role of TPP, a mitochondria-targeting molecule. A commonly used mitochondrial dye, Mito-Tracker Green (MTG), was employed to label mitochondria for the imaging observation. As exhibited in Fig. 5A, a much stronger fluorescence signal was found in MCF-7 cells in the TPP-INP group than that in the INP group for 6 h. The flow cytometric fluorescent quantitation further confirmed that the TPP modification significantly accelerated the internalization of the nanoparticles due to the great binding affinity to the inner mitochondrial membranes (Fig. 5B). Fig. 5C demonstrated the mitochondria-targeted delivery at higher resolution. The obtained results confirmed that the TPP mediated mitochondria-targeting could effectively enhance the accumulation in mitochondria.

To calculate the amount of singlet oxygen produced by celastrol, the flow cytometer was employed to quantitative analyze the intracellular ROS (Fig. 6). According to reports, cytotoxic ROS can damage the mitochondria in cells, resulting in cell death.[60] The ROS generated in MCF-7 cells when treating with celastrol and ICG loaded nanopaticles (Cet@Fc-INPs), TPP–Cet and ICG loaded particles (TPP–Cet@Fc-INPs) and RA–Pt/TPP–Cet@Fc-INPs, were evaluated by using a DCFH-DA probe. The MCF-7 cells were treated with DCFH-DA as the control group. As the results exhibited, the fluorescence intensities of positive cells increased to 63.1% after being treated with Cet@Fc-INPs. Moreover, the fluorescence intensities of positive cells increased to 79.0% when incubating with TPP–Cet@Fc-INPs, while it reached 83.2% in the RA–Pt/TPP–Cet@Fc-INP group. Compared to single TPP–Cet loaded nanoparticles, the RA–Pt and TPP–Cet dual loaded nanoparticles showed stronger cytotoxicity and thus lead to more ROS accumulation. The results further highlight the synergistic anti-cancer therapy as compared with single therapy. In addition, the obtained results highlighted the TPP mediated mitochondrial targeting and the subsequent ROS accumulation in mitochondria.

3.7 Cytotoxicity *in vitro*

The cytotoxicity is the primary consideration when designing a novel nano-therapeutic agent. Before the experiment, the IC_{50} (μmol L^{-1}) values for MDA-MB-231, and MCF-7 cell lines were investigated and the results are shown in Table S2 (ESI†). As expected, both pro-drug molecules (RA–Pt and TPP–Cet) showed enhanced toxicity to selected cell lines when compared

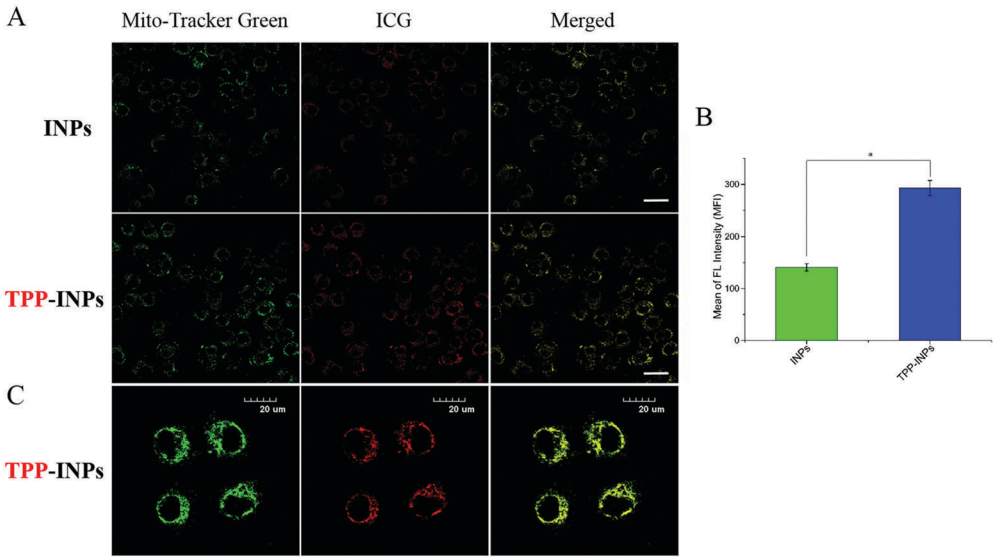

Fig. 5 (A) Internalization of the ICG-labeled targeted nanoparticles (TPP-INPs) or nanoparticles without TPP ligands (INPs) (equivalent to 50.0 μg mL^{-1} ICG) by MCF-7 cells for 6 h, analyzed by CLSM (scale bar, 40 μm). (B) Flow cytometric analyses of MCF-7 cells after 6 h of incubation with ICG-loaded nanoparticles (equivalent to 50 μg mL^{-1} ICG) in the presence or absence of TPP. Data are presented as the mean ± SD (n = 3, $*P < 0.05$, $**P < 0.01$). (C) Internalization of the ICG-labeled targeted nanoparticles (TPP-INPs) (equivalent to 50.0 μg mL^{-1} ICG) by MCF-7 cells for 6 h, analyzed by CLSM (scale bar, 20 μm).

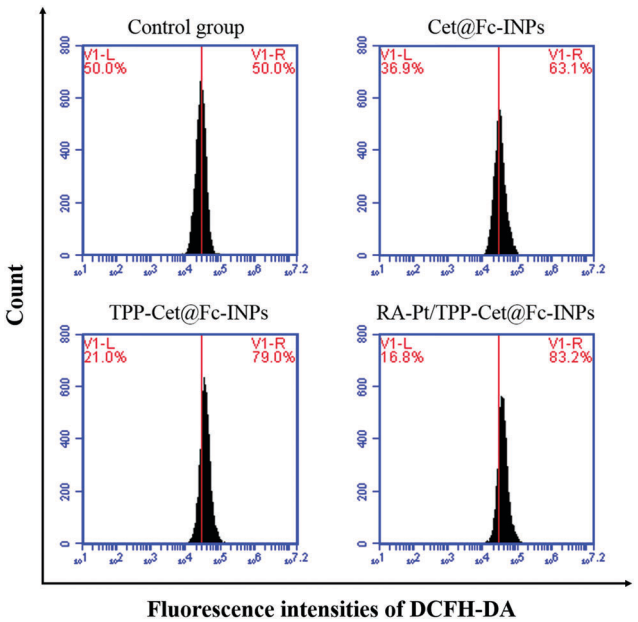

Fig. 6 The fluorescence intensities of DCFH-DA in MCF-7 cells after being treated with Cet@Fc-INPs, TPP–Cet@Fc-INPs and RA–Pt/TPP–Cet@Fc-INPs (48.0 μg mL^{-1}) for 12 h; the medium was used as the control group.

with single molecules without modification. Then the cytotoxicity of RA–Pt/TPP–Cet@Fc-INPs was evaluated in MDA-MB-231 and MCF-7 cells using standard MTT assay. As shown in Fig. 7A, the MDA-MB-231 cells treated with RA–Pt/TPP–Cet@Fc-INPs and further treated with NIR irradiation did not show a significant difference in cell viability when compared with the control group, hollow nanoparticles (blank Fc-NPs), free RA–Pt, RA–Pt and TPP–Cet dual loaded nanoparticles without targeted ligands (RA–Pt/TPP–Cet@INPs) or even RA–Pt/TPP–Cet@Fc-INPs without NIR irradiation at a RA–Pt concentration below 1.0 μg mL^{-1}. However, the cell viability of the RA–Pt/TPP–Cet@Fc-INPs with added NIR irradiation group decreased obviously, and that treated with blank Fc-NPs showed little difference as the RA–Pt concentration reached 10.0 μg mL^{-1}. Moreover, the obtained results showed that the cell viability of RA–Pt/TPP–Cet@INPs (10.0 μg mL^{-1}) reached 28.86%, which was 25.32% lower than that in the free RA–Pt group (54.18%), showing the expected synergistic effect. To compare the cell-killing performance of RA–Pt/TPP–Cet@Fc-INPs, the MCF-7 cells, which overexpress the folate receptor, were further evaluated and the results are shown in Fig. 7B.

As shown in Fig. 7B, the low concentration (0.1 μg mL^{-1}) of RA–Pt did not show a remarkable effect on the viability of MCF-7 cells as compared with the free RA–Pt group, RA–Pt/TPP–Cet@INP group or RA–Pt/TPP–Cet@Fc-INP without NIR irradiation group. However, after irradiation with the NIR laser (808 nm, 1.54 W), the cell viability of RA–Pt/TPP–Cet@Fc-INPs (1.0 μg mL^{-1}) reduced from 56.43% to 38.73%, and the cell viability of RA–Pt/TPP–Cet@Fc-INPs (5.0 μg mL^{-1}) further reduced to 22.41% after being exposed to the NIR laser. Besides, simultaneous incubation with RA–Pt and TPP–Cet (RA–Pt/TPP–Cet@INPs, 10.0 μg mL^{-1}, 26.53%) had much better inhibitory effects on cells than that in the single drug group (free RA–Pt, 10.0 μg mL^{-1}, 48.80%), further confirming the expected synergistic effect. Specifically, the inhibition rate of MCF-7 cells incubated with RA–Pt/TPP–Cet@Fc-INPs (10.0 μg mL^{-1}) with added NIR irradiation for 5 min reached 96.97%, which showed the great potential as a new type of NIR-responsive drug release for cancer therapy.

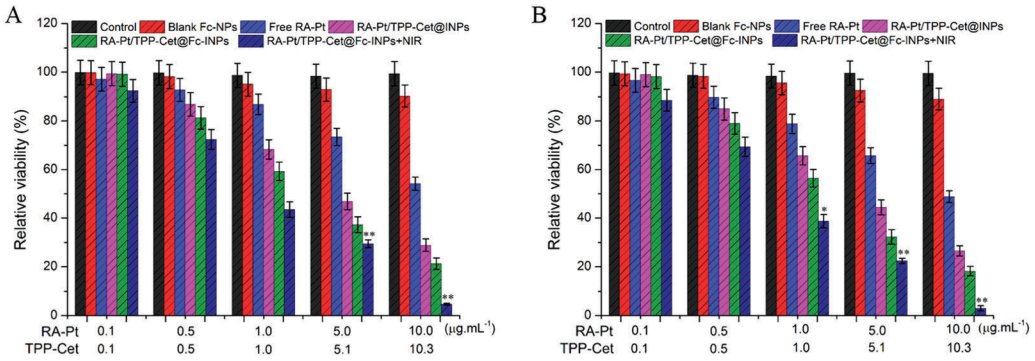

Fig. 7 Quantitative evaluation of cell viability for MDA-MB-231 cells (A) and MCF-7 cells (B) treated with PBS, blank Fc-INPs, free RA–Pt, RA–Pt/TPP–Cet@INPs, and RA–Pt/TPP–Cet@Fc-INPs with NIR irradiation (+, –) for 24 h. Error bars were based on the standard error of the mean (n = 3). N.S.: no significance; *$P < 0.05$; ** $P < 0.01$ based on Student's t test.

Due to the dual targeting effect of folate and cRGD, the drug carriers can be internalized in large quantities by tumor cells. The obtained results indicated that the co-delivery of two different antitumor agents can effectively enhance the therapeutic efficiency and our study highlighted the synergistic anticancer therapy. In addition, according to reports,[61,62] the range

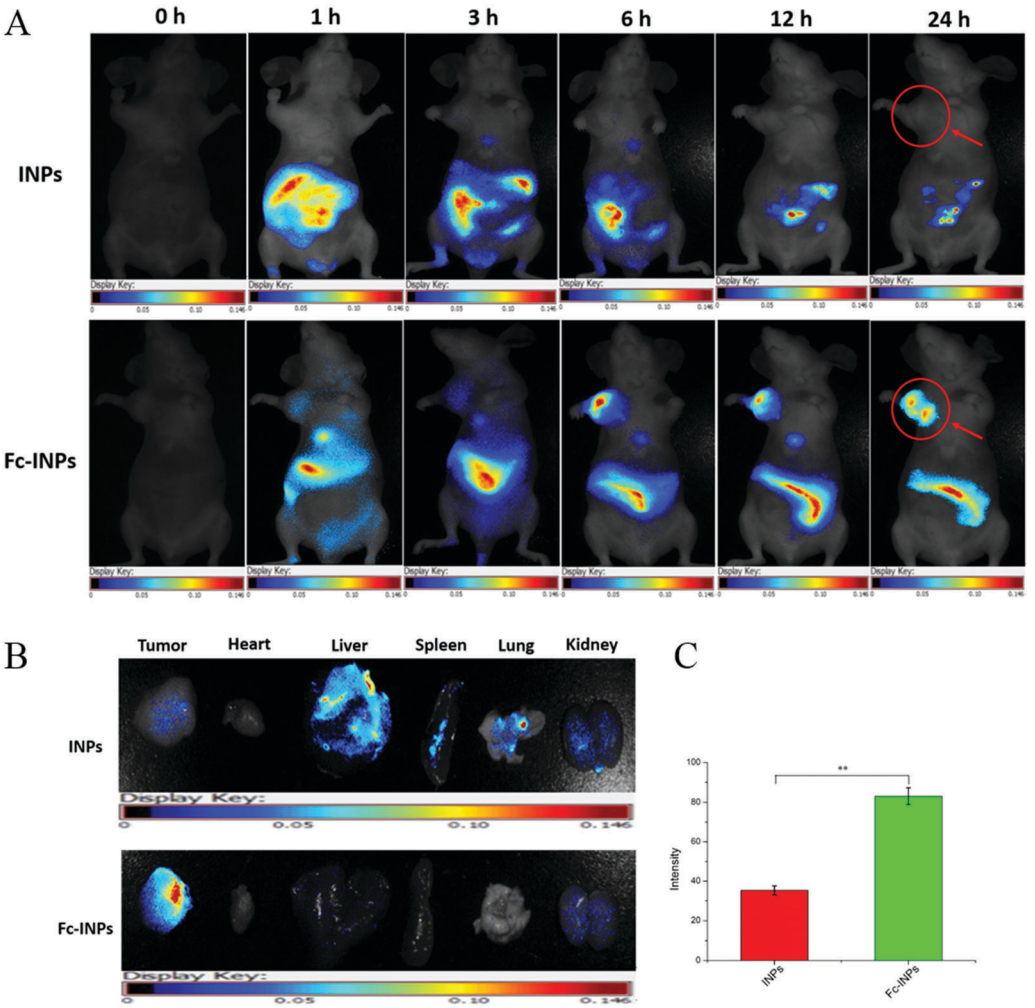

Fig. 8 (A) *In vivo* fluorescence imaging of subcutaneous MCF-7 breast tumor-bearing nude mice after intravenous injection of nanoparticles. (B) Images of dissected organs of mice bearing subcutaneous MCF-7 breast tumors sacrificed 24 h after intravenous injection of nanoparticles. (C) Flow cytometric analysis of the ICG fluorescence intensity in MCF-7 breast tumors incubated with INPs or Fc-INPs for 24 h. Data are presented as the mean ± SD (n = 3, *$p < 0.05$, **$p < 0.01$).

of temperatures within which the drug-delivery system is activated, should be keep between 37 and 42 °C, because temperatures beyond this range will cause protein denaturation or function disruption. In the current study, the prepared blank nanoparticles did not cause significant cytostatic effects under NIR irradiation, indicating that the prepared nanoparticles did not induce high internal temperatures under current NIR irradiation conditions. In this way, the designed nanopharmaceutical system does not harm normal cells and shows great potential for application.

3.8 Drug delivery and *in vivo* imaging

On the basis of the *in vitro* cytotoxicity results, we further applied the RA–Pt/TPP–Cet@Fc-INPs to mice for ICG imaging *in vivo*. The fluorescence signals were recorded at different time intervals (Fig. 8A).

As shown in Fig. 8A, the fluorescence signals of the tumor site in the Fc-INP group were obviously stronger at any time post-injection ranging from 1 h to 24 h. Moreover, the fluorescence signals of the INP group were majorly distributed in the liver but less in the tumor during 1 h after injection, while the fluorescence signals of the Fc-INP group homogeneously distribute in the whole body. We have further noticed that the fluorescence signals in the tumor (Fc-INP group) were gradually strengthened with the time increasing (0, 1, 3, 6, 12 and 24 h) and reached a maximum in 24 h after Fc-INP solution injection while these signals in the INP group completely disappeared in 24 h after injection. Overall, the Fc-INP group showed much stronger fluorescence in the tumor site than that of the INP group, confirming the specific targeting of Fc-INPs *in vivo*.

Fluorescence imaging *in vivo* was further performed to investigate the nanoparticle distribution in various organs. The distributions of INPs or Fc-INPs in major organs and tumors 24 h post-injection are shown in Fig. 8B. The fluorescence signals were easily observed in the tumor site of the mice treated with Fc-INPs, while much weaker signals were collected in the INP group. Moreover, the fluorescence signals of the Fc-INP group in the five organs (heart, liver, spleen, lung, and kidney) were hardly observed except those in the liver and kidney. In addition, the fluorescence signals accumulated in the liver were much weaker when treating with Fc-INPs. Since the prepared nanoparticles conjugate with folate and cRGD ligands, which have greatly enhanced the specificity of tumor cells. Therefore, the fluorescence signals in the tumor were particularly significant in the Fc-INP group. The *in vivo* fluorescence signals of the tumors 24 h post-injection of the INP or Fc-INP solutions were quantified and the results indicated the obvious difference (Fig. 8C). Thus, the prepared Fc-INPs showed enhanced accumulation in the tumor site due to the conjugation of folate and cRGD.

3.9 *In vivo* combinational therapeutic efficacy

We further applied the RA–Pt/TPP–Cet@Fc-INPs to mice for enhanced antitumor therapy *in vivo*. According to the results of *in vivo* FL imaging of ICG, synergistic therapy was performed at the time point of 24 h post-injection.

As shown in Fig. 9, the control, or free RA–Pt group, showed rapid tumor growth, indicating that the tumor growth was affected by the biocompatible carrier. The tumor suppression of RA–Pt/TPP–Cet@INPs or the RA–Pt/TPP–Cet@Fc-INP group

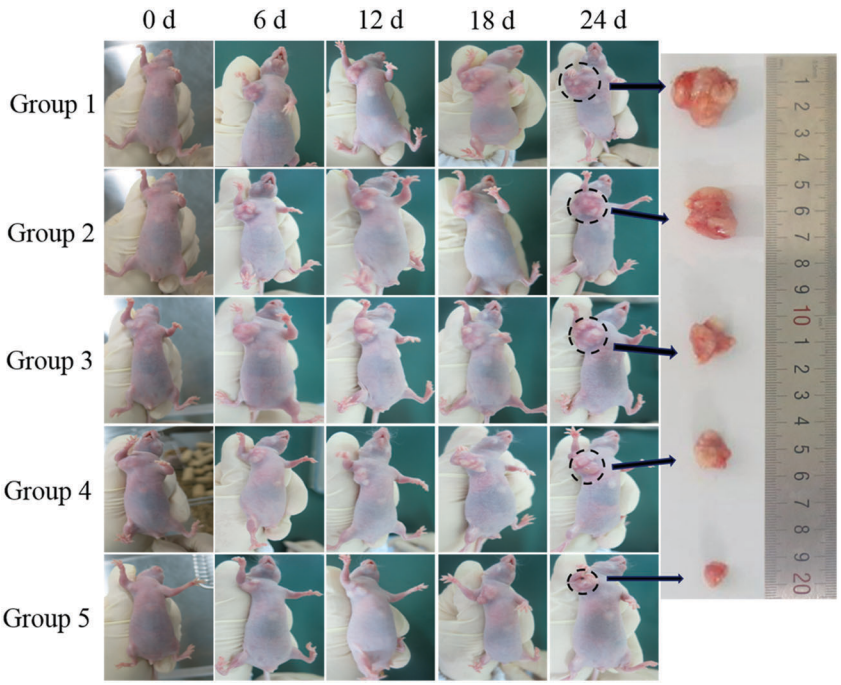

Fig. 9 Representative photographs of mice bearing MCF-7 breast tumors treated with PBS solution (group 1), free RA–Pt (group 2), RA–Pt/TPP–Cet@INPs (group 3), RA–Pt/TPP–Cet@Fc-INPs (group 4), and RA–Pt/TPP–Cet@Fc-INPs + NIR (group 5).

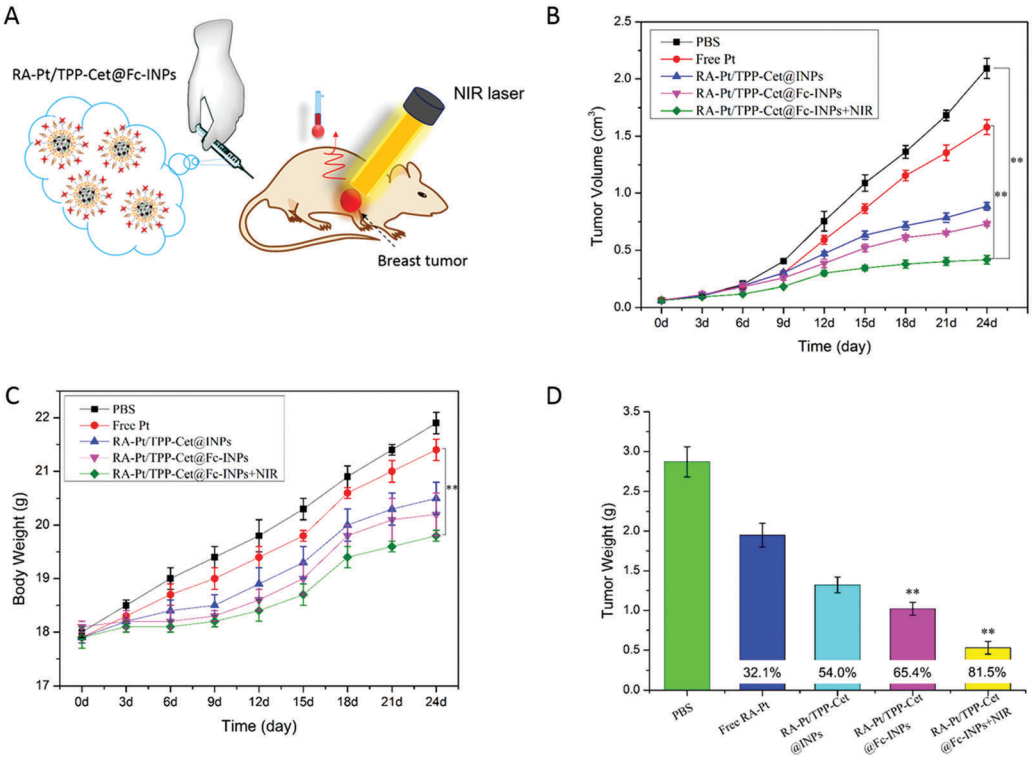

Fig. 10 *In vivo* antitumor activity on solid tumors using female BABL/c nude mice based MCF-7 breast tumor models. (A) Scheme of combined therapy of live MCF-7 breast tumor-bearing nude mice treated with RA–Pt/TPP–Cet@Fc-INP suspensions under 808 nm laser irradiation. (B) Relative tumor volume growth curves in different groups of tumor-bearing mice after various treatments (were normalized to their initial sizes). (C) Tumor weight growth curves in different groups of tumor-bearing mice after various treatments. Asterisk indicates $p < 0.01$. Error bars represent the standard deviation of six mice per group. (D) The tumor weight in different groups of tumor-bearing mice after incubation for 28 days. Data are presented as the mean ± SD ($n = 6$, $*p < 0.05$, $**p < 0.01$ *vs.* PBS group).

without NIR irradiation did not show a remarkable difference, while the RA–Pt/TPP–Cet@Fc-INP group with NIR irrradiation caused significant inhibition after 24 days (Fig. 9). Additionally, during the 24 days of treatment, the tumor volume increased significantly in the PBS group (Fig. 10B), and the RA–Pt/TPP–Cet@Fc-INP group exhibited an 81.5% tumor inhibition rate after 24 days (Fig. 10D). During the 3 days of treatment, no significant body weight change was observed in all groups (Fig. 10C), showing that RA–Pt/TPP–Cet@Fc-INPs without NIR irradiation had no significant side effects on the treated mice *in vivo*. During the treatment period, the body weight of mice in group 1 (the control group) increased by 3.9 g, while that in groups 2, 3, and 4 also increased by 3.5 g, 2.6 g, and 2.1 g, respectively. However, the body weight of the RA–Pt/TPP–Cet@Fc-INP group with NIR (group 5) only increased by 1.9 g, considering that the tumor volume of the mice decreased from group 1 to group 5 in turn, indicating that the mice in group 5 were increased in normal body weight and the prepared nanoparticles showed a good anti-tumor effect. Therefore, the obtained results highlighted the NIR-responsive drug release and great potential in application for tumor inhibition.

Next, the tumors and normal organs were analyzed by H&E staining to further investigate the potential toxicity of RA–Pt/TPP–Cet@Fc-INPs. The PBS group (group 1) clearly showed tumor necrosis and destroyed blood vessels, while the free

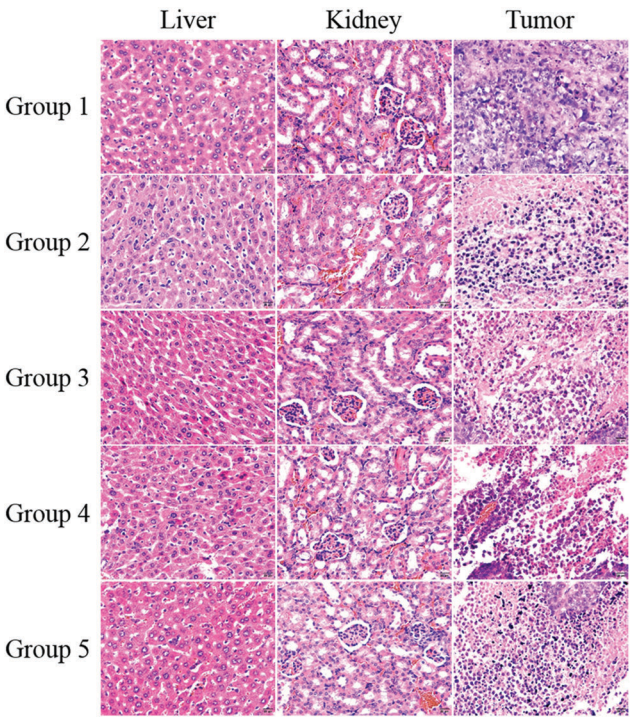

Fig. 11 H&E stained images of major organs from mice treated with PBS solution (group 1), free RA–Pt (group 2), RA–Pt/TPP–Cet@INPs (group 3), RA–Pt/TPP–Cet@Fc-INPs (group 4), and RA–Pt/TPP–Cet@Fc-INPs + NIR (group 5).

RA–Pt group (group 2) induced moderate levels of tumor necrosis (Fig. 11). By contrast, no significant tumor destruction was observed in the other three control groups. The results indicated that compared with the control group (group 1 and 2), the morphologies of the tumor cells in nanoparticle-administered groups (group 3, 4 and 5) were better, and the blood vessels and other functions were restored to different degrees.

The H&E images of major detoxification organs (liver and kidney) from MCF-7 tumor-bearing mice showed that there was no obvious organ damage or inflammation lesions induced by the applied synergistic therapy in all groups (Fig. 11). These obtained results clearly demonstrated that the RA–Pt/TPP–Cet@Fc-INPs have high biocompatibility and specificity, and can be considered as a nanotheranostic agent for imaging-guided synergistic therapy of cancer.

4. Conclusion

In summary, we successfully developed a biocompatible, folate and cRGD dual-targeted nanotheranostic agent for synergistic cancer therapy. The prepared RA–Pt/TPP–Cet@Fc-INPs showed low cytotoxicity, a high capacity for RA–Pt and TPP–Cet loading, and the ability to target MCF-7 cells or to induce ROS. The RA and TPP mediated subcellular targeting, and ICG imaging-guided synergistic therapy using RA–Pt/TPP–Cet@Fc-INPs induced significant tumor cell death *in vitro*, and efficiently inhibited the MCF-7 tumor growth *in vivo*. These results demonstrate the potential theranostic efficacy of RA–Pt/TPP–Cet@Fc-INPs for the synergistic treatment of solid tumors, thus offering a new approach for multistage targeted-delivery and synergistic therapy based on functional nanomedicines.

Conflicts of interest

There are no conflicts to declare.

Acknowledgements

We are highly grateful to the International S&T Cooperation Program of China (No. 2015DFG42240), the financial support from the National Natural Science Foundation of China (Grant No. 21628101 and 21371031), The Technological Program Foundation of Jiangsu Province (No. BY2015070-09), and the Priority Academic Program Development (PAPD) of Jiangsu Higher Education Institutions.

References

1 N. A. Ochekpe, P. O. Olorunfemi and N. C. Ngwuluka, *Trop. J. Pharm. Res.*, 2009, **8**, 377–390.
2 S. E. Leucuta, *Curr. Clin. Pharmacol.*, 2010, **5**, 257–280.
3 S. Singh, *J. Nanosci. Nanotechnol.*, 2010, **10**, 7906–7918.
4 R. S. Raghuvanshi, Y. K. Katare, K. Lalwani, M. M. Ali, O. Singh and A. K. Panda, *Int. J. Pharm.*, 2002, **245**, 109–121.
5 J. Kreuter, V. E. Petrov, D. A. Kharkevich and R. N. Alyautdin, *J. Controlled Release*, 1997, **49**, 81–87.
6 F. Alexis, E. Pridgen, L. K. Molnar and O. C. Farokhzad, *Mol. Pharmaceutics*, 2008, **5**, 505–515.
7 N. Toub, C. Malvy, E. Fattal and P. Couvreur, *Biomed. Pharmacother.*, 2006, **60**, 607–620.
8 M. Zeira, P. F. Tosi, Y. Mouneimne, J. Lazarte, L. Sneed, D. J. Volsky and C. Nicolau, *Proc. Natl. Acad. Sci. U. S. A.*, 1991, **88**, 4409–4413.
9 S.-I. Hamano, S. Yamashita, M. Tanaka, S. Yoshinari, M. Minamitani and Y. Eto, *J. Pediatr.*, 2006, **148**, 485–488.
10 H. Padh and N. M. Sakhrani, *Drug Des., Dev. Ther.*, 2013, **7**, 585–599.
11 A. R. Maity and D. Stepensky, *Int. J. Pharm.*, 2015, **496**, 268–274.
12 L. Rajendran, H.-J. Knölker and K. Simons, *Nat. Rev. Drug Discovery*, 2010, **9**, 29–42.
13 S. Balaz, *Chem. Rev.*, 2009, **109**, 1793–1899.
14 G. G. D'Souza and V. Weissig, *Expert Opin. Drug Delivery*, 2009, **6**, 1135–1148.
15 V. Escriou, M. Carriere, D. Scherman and P. Wils, *Adv. Drug Delivery Rev.*, 2003, **55**, 295–306.
16 J. Zhong, L. Li, X. Zhu, S. Guan, Q. Yang, Z. Zhou, Z. Zhang and Y. Huang, *Biomaterials*, 2015, **65**, 43–55.
17 R. J. Sessler and N. Noy, *Mol. Cell*, 2005, **18**, 343–353.
18 A. Majumdar, A. D. Petrescu, Y. Xiong and N. Noy, *J. Biol. Chem.*, 2011, **286**, 42749–42757.
19 A. A. Argyriou, P. Polychronopoulos, G. Iconomou, E. Chroni, P. Haralabos and H. P. Kalofonos, *Cancer Treat. Rev.*, 2008, **34**, 368–377.
20 S. R. McWhinney, R. M. Goldberg and H. L. McLeod, *Mol. Cancer Ther.*, 2009, **8**, 10–16.
21 G. Daugaard and U. Abildgaard, *Cancer Chemother. Pharmacol.*, 1989, **25**, 1–9.
22 S. Kotecha, *Biochim. Biophys. Acta, Mol. Basis Dis.*, 2010, **1802**, 649–658.
23 Y. Yamada and H. Harashima, *Adv. Drug Delivery Rev.*, 2008, **60**, 1439–1462.
24 P. I. Moreira, M. S. Santos and C. R. Oliveira, *Antioxid. Redox Signaling*, 2007, **9**, 1621–1630.
25 T. Finkel, *Nat. Rev. Mol. Cell Biol.*, 2006, **6**, 971.
26 G. Chen, X. Zhang, M. Zhao, Y. Wang, X. Cheng, D. Wang, Y. J. Xu, Z. Y. Du and X. D. Yu, *BMC Cancer*, 2011, **11**, 170.
27 J. H. Lee, Y. S. Won, K. H. Park, M. K. Lee, H. Tachibana, K. Yamada and K. I. Seo, *Apoptosis*, 2012, **17**, 1275–1286.
28 H. Mou, Y. Zheng, P. Zhao, H. Bao, W. Fang and N. Xu, *Toxicol. In Vitro*, 2011, **25**, 1027–1032.
29 H. Padh and N. M. Sakhrani, *Drug Des., Dev. Ther.*, 2013, **7**, 585–599.
30 G. G. D'Souza, M. A. Wagle, V. Saxena and A. Shah, *Biochim. Biophys. Acta, Bioenerg.*, 2011, **1807**, 689–696.
31 J. Zhou, W.-Y. Zhao, X. Ma, R.-J. Ju, X.-Y. Li, N. Li, M.-G. Sun, J.-F. Shi, C.-X. Zhang and W.-L. Lu, *Biomaterials*, 2013, **34**, 3626–3638.
32 D. Y. Cho, H. Cho, K. Kwon, M. Yu, E. Lee, K. M. Huh, D. H. Lee and H. C. Kang, *Adv. Funct. Mater.*, 2015, **25**, 5479–5491.

33 L. F. Yousif, K. M. Stewart, K. L. Horton and S. O. Kelley, *ChemBioChem*, 2009, **10**, 2081–2088.
34 K. L. Horton, K. M. Stewart, S. B. Fonseca, Q. Guo and S. O. Kelley, *Chem. Biol.*, 2008, **15**, 375–382.
35 Z. Khatun, Y. S. Choi, Y. G. Kim, K. Yoon, M. Nurunnabi, L. Li, E. Lee, H. C. Kang and K. M. Huh, *Biomacromolecules*, 2017, **18**, 1074–1085.
36 E. Ju, Z. Li, Z. Liu, J. Ren and X. Qu, *ACS Appl. Mater. Interfaces*, 2014, **6**, 4364–4370.
37 P. A. Ascierto and F. M. Marincola, *J. Transl. Med.*, 2011, **9**, 115.
38 C. Zhu, S. Jung, S. Luo, F. Meng, X. Zhu, T. G. Park and Z. Zhong, *Biomaterials*, 2010, **31**, 2408–2416.
39 S. H. Lee, J. K. Ryu, K. Y. Lee, S. M. Woo, J. K. Park, J. W. Yoo, Y. T. Kim and Y. B. Yoon, *Cancer Lett.*, 2008, **259**, 39–49.
40 D. W. Ahn, J. K. Seo, S. H. Lee, J. H. Hwang, J. K. Lee, J. K. Ryu, Y. T. Kim and Y. B. Yoon, *Pancreas*, 2012, **41**, 1048–1057.
41 B. Yao, Q. M. He, L. Tian, F. Xiao, Y. Jiang, R. Zhang, G. Li, L. Zhang, J. M. Hou, L. Wang, X. C. Cheng, Y. J. Wen, B. Kan, J. Li, X. Zhao, B. Hu, Q. Zhou, L. Zhang and Y. Q. Wei, *Hum. Gene Ther.*, 2005, **16**, 1075–1086.
42 C. Q. You, H. S. Wu, M. X. Wang, Y. W. Zhang, J. W. Wang, Y. H. Luo, L. H. Zhai, B. W. Sun, X. Y. Zhang and J. Zhu, *Chem. – Eur. J.*, 2017, **23**, 5352–5360.
43 C. Q. You, H. S. Wu, M. X. Wang, Z. G. Gao, B. W. Sun and X. Y. Zhang, *Mater. Sci. Eng., C*, 2018, **92**, 453–462.
44 C. Q. You, M. X. Wang, H. S. Wu, P. J. An, M. M. Pan, Y. H. Luo and B. W. Sun, *Mater. Sci. Eng., C*, 2017, **80**, 362–370.
45 Y. M. Zhang, F. Huang, C. H. Ren, L. J. Yang, J. F. Liu, Z. Cheng, L. P. Chu and J. J. Liu, *ACS Appl. Mater. Interfaces*, 2017, **9**, 13016–13028.
46 S. T. Mayne, H. A. Risch, R. Dubrow, W.-H. Chow, M. D. Gammon, T. L. Vaughan, D. C. Farrow, J. B. Schoenberg, J. L. Stanford, H. Ahsan, A. B. West, H. Rotterdam, W. J. Blot and J. F. Fraumeni Jr, *Cancer Epidemiol., Biomarkers Prev.*, 2001, **10**, 1055–1062.
47 A. Shibata, T. Nagaya, T. Imai, H. Funahashi, A. Nakao and H. Seo, *Breast Cancer Res. Treat.*, 2002, **73**, 237–243.
48 J. Renukuntla, S. Shah, S. H. S. Boddu, A. D. Vadlapudi, R. K. Vadlapatla, D. Pal and A. K. Mitra, *Drug Dev. Ther.*, 2015, **6**, 52–61.
49 Y. Y. Zhang, C. Teh, M. H. Li, C. Y. Ang, S. Y. Tan, Q. Y. Qu, V. Korzh and Y. L. Zhao, *Chem. Mater.*, 2016, **28**, 7039–7050.
50 H. Ranji-Burachaloo, F. Karimi, K. Xie, Q. Fu, P. A. Gurr, D. E. Dunstan and G. G. Qiao, *ACS Appl. Mater. Interfaces*, 2017, **9**, 33599–33608.
51 C. Q. You, H. S. Wu, M. X. Wang, S. L. Wang, T. Y. Shi, Y. H. Luo, B. W. Sun, X. Y. Zhang and J. Zhu, *Nanotechnology*, 2017, **28**, 165102.
52 C. Q. You, H. S. Wu, M. X. Wang, Z. G. Gao, X. Y. Zhang and B. W. Sun, *Nanotechnology*, 2018, **29**, 015601.
53 H. S. Choi, W. Liu, P. Misra, E. Tanaka, J. P. Zimmer, B. I. Ipe, M. G. Bawendi and J. V. Frangioni, *Nat. Biotechnol.*, 2007, **25**, 1165–1170.
54 M. Dellian, F. Yuan, V. S. Trubetskoy, V. P. Torchilin and R. K. Jain, *Br. J. Cancer*, 2000, **82**, 1513–1518.
55 C. Fang, B. Shi, Y. Y. Pei, M. H. Hong, J. Wu and H. Z. Chen, *Eur. J. Pharm. Sci.*, 2006, **27**, 27–36.
56 D. C. Perrault, C. Walkey, T. Jennings, H. C. Fischer and W. C. W. Chan, *Nano Lett.*, 2009, **9**, 1909–1915.
57 F. Danhier, A. L. Breton and V. Preat, *Mol. Pharmaceutics*, 2012, **9**, 2961–2973.
58 C. Q. You, J. Yu, Y. Sun, Y. H. Luo, X. Y. Zhang, J. Zhu and B. W. Sun, *New J. Chem.*, 2017, **41**, 773–785.
59 Q. Q. Yang, L. Wu, L. Li, Z. Zhou and Y. Huang, *Nanoscale*, 2017, **9**, 1547.
60 Y. L. Chang, S. T. Yang, J. H. Liu, E. Dong, Y. W. Wang, A. Cao, Y. F. Liu and H. F. Wang, *Toxicol. Lett.*, 2011, **200**, 201–210.
61 M. H. Xiong, Y. Bao, X. Z. Yang, Y. C. Wang, B. Sun and J. Wang, *J. Am. Chem. Soc.*, 2012, **134**, 4355–4362.
62 M. Tanihara, Y. Suzuki, Y. Nishimura, K. Suzuki, Y. Kakimaru and Y. Fukunisi, *J. Pharm. Sci.*, 1999, **88**, 510–514.

